Journal of Energy Storage 85 (2024) 110954

Contents lists available at ScienceDirect

Journal of Energy Storage

journal homepage: www.elsevier.com/locate/est

Research papers

Improving phase change heat transfer in an enclosure filled by uniform and heterogenous metal foam layers: A neural network design approach

Hakim S. Sultan [a], Mohammed Hasan Ali [b], Jana Shafi [c], Mehdi Fteiti [d], Manuel Baro [e], Faisal Alresheedi [f], Mohammad S. Islam [g], Talal Yusaf [h,i], Mohammad Ghalambaz [i,*]

[a] College of Engineering, University of Warith Al-Anbiyaa, Karbala 56001, Iraq
[b] College of Technical Engineering, Imam Ja'afar Al-Sadiq University, Al-Muthanna 66002, Iraq
[c] Department of Computer engineering and information, College of Engineering in Wadi Alddawasir, Prince Sattam Bin Abdulaziz University, Wadi Alddawasir 11991, Saudi Arabia
[d] Physics Department, Faculty of Science, Umm Al-Qura University, Makkah 24381, Saudi Arabia
[e] Tecnológico Nacional de México Campus Nuevo Casas Grandes, Nuevo Casas Grandes, Chih., Mexico
[f] Department of Physics, College of Science, Qassim University, Buraidah 51452, Saudi Arabia
[g] School of Mechanical and Mechatronic Engineering, Faculty of Engineering and Information Technology, University of Technology Sydney, Ultimo, NSW 2007, Australia
[h] School of Engineering and Technologies, Central Queensland University, Rockhampton, QLD 4701, Australia
[i] College of Engineering, Almaaqal University, Basra 61003, Iraq

ARTICLE INFO

Keywords:
Heterogeneous metal foam
Neural networks
Phase change material (PCM)
Latent heat thermal energy storage (LHTES)
Melting process

ABSTRACT

Phase change materials (PCMs) inherently store and release large amounts of energy during phase transitions. In this research, the potential of two metal foam (MF) layers in enhancing the thermal energy storage unit's heat transfer was probed, with one layer having distinct attributes at an anisotropic angle, ω. Utilizing the finite element method to understand the system dynamics, model accuracy was affirmed through rigorous checks. The impact of the heterogeneous parameter ($0 < Kn < 0.3$), heterogeneous angle ($0 < \omega < 90°$), and porosity $0.9 < \varepsilon < 0.975$ was addressed on the melting process. To circumvent the high simulation costs, an artificial neural network (ANN) was trained on 7838 data points. Noteworthy findings indicate that a slight 7.5 % increase in porosity can reduce the melting time by 66 %. Moreover, the 0° anisotropic angle emerged as the most efficient in heat transfer due to its superior thermal properties. The incorporation of ANN analytics was a pivotal shift, bypassing the traditionally high computational demands of phase change heat transfer studies. Once fully trained, the ANN adeptly demonstrated melting volume fraction (MVF) nuances under varied conditions. Further, optimal melting efficiencies were pinpointed at the $\omega = 0°$ angle, with a specific porosity zone, $\varepsilon \sim 0.925$, showing minimal MVF and the benefits of a higher porosity ($\varepsilon = 0.94$) becoming evident at $t = 3000$ s. Ultimately, this investigation harmoniously integrates traditional analytical tools with ANN technology, offering profound insights into PCM heat transfer dynamics and laying the groundwork for future energy-efficient thermal storage solutions.

1. Introduction

As the race toward energy efficiency and thermal optimization intensifies, applying and understanding advanced heat transfer mechanisms are paramount. Thanks to their impressive latent heat storage capacities, phase change materials (PCMs) have developed as a front-runner in the world of thermal management. However, despite their potential, there is an ongoing challenge in maximizing their heat transfer rate during phase change processes [1,2]. Introducing metal foams—a porous medium with the power to dramatically enhance heat transfer rates [3]. By looking into enclosures partially filled by metal foam layers, researchers and engineers are now unlocking new dimensions in phase change heat transfer optimization [3,4]. This article delves into the intricacies of these foam layers, their interactions with

* Corresponding author.
E-mail addresses: hakim.s@uowa.edu.iq (H.S. Sultan), mohammed.hasan@sadiq.edu.iq (M.H. Ali), j.jana@psau.edu.sa (J. Shafi), mafteiti@uqu.edu.sa (M. Fteiti), mbaro@itsncg.edu.mx (M. Baro), mohammadsaidul.islam@uts.edu.au (M.S. Islam), t.yusaf@cqu.edu.au (T. Yusaf), m.ghalambaz@gmail.com (M. Ghalambaz).

https://doi.org/10.1016/j.est.2024.110954
Received 18 October 2023; Received in revised form 9 February 2024; Accepted 12 February 2024
2352-152X/© 2024 Elsevier Ltd. All rights reserved.

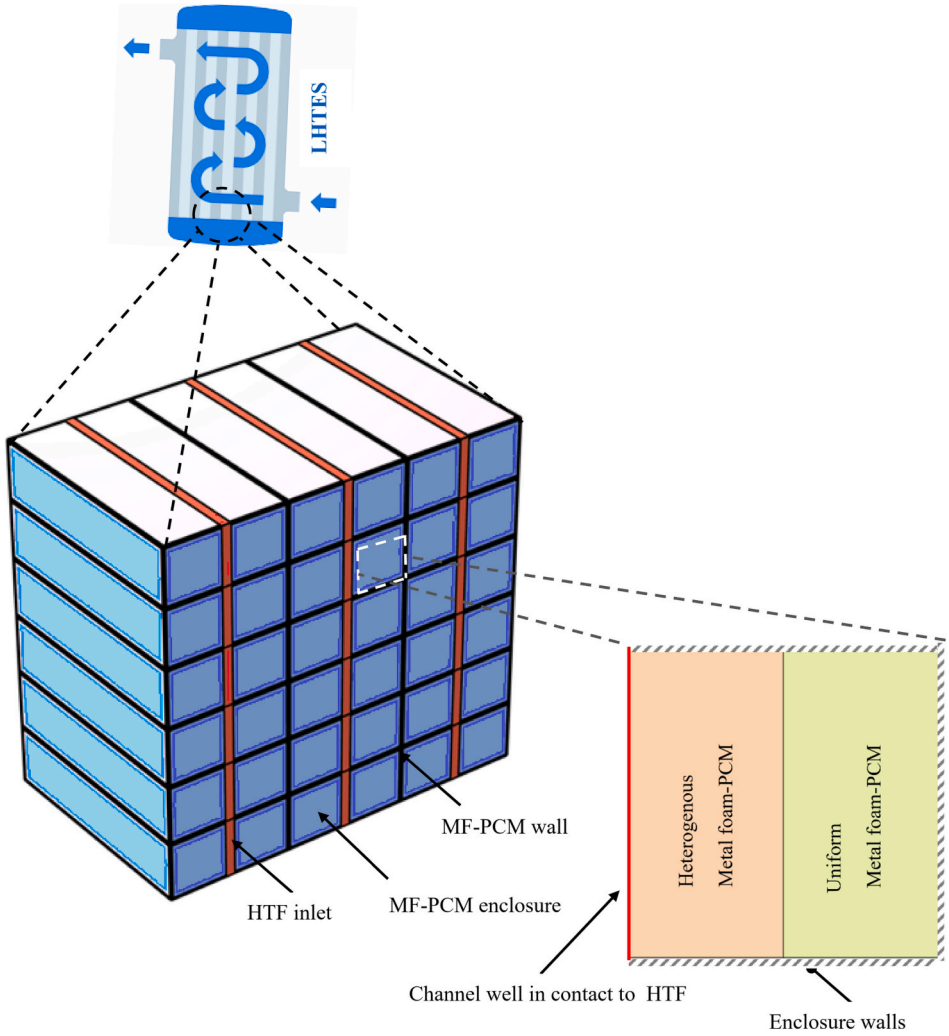

Fig. 1. A schematic view of an LHTES unit and channel shape PCM containers.

PCMs, and the groundbreaking heterogeneous metal foam for heat transfer enhancement.

Latent heat thermal energy storage (LHTES) paired with metal foams is emerging as a groundbreaking technology in heat transfer and energy storage [5,6]. With the increasing global demand for sustainable and efficient energy solutions, this combination promises to reshape sectors ranging from building design [7] to electronics cooling [8,9].

Focusing on energy recovery from domestic radiators, the study of Sardari et al. [10] demonstrated the potential of a compact LHTES unit placed on the wall side surface of domestic radiators. This system captures otherwise wasted energy and utilizes a porous medium for heat storage and retrieval, resulting in a quicker charging time, approximately 95 % of the corresponding time for charging the PCM-only alternative. Furthermore, the study posited the superiority of higher porosity (97 %) systems for maintaining nearly constant surface temperatures. In a different realm, aiming [11] at dwelling space air heating, numerical studies have shown the advantages of a composite metal foam/PCM-air heat exchanger over its PCM-only counterpart. Notably, the composite reduced discharging time by 56.5 % and provided a consistent output temperature. These results spotlight the importance of specific geometrical parameters in optimizing heat transfer. Yet another study explored the impact of integrating a PCM-metal foam composite on the charging/discharging processes of bundled-tube LHTES units [12]. The use of metal foams (MFs) to enhance the thermal conductivity of the PCM proved instrumental in achieving efficient heat transfer. This resulted in improved melting and solidification processes, thereby making the overall system both easily configurable and efficient.

An intriguing approach considered the geometry modification to understand its impact on the thermal response of composite MF-PCM for thermal energy storage [13]. Findings of [13] suggest that geometry modification might hold the key to more efficient thermal responses. Specifically, the conical shell system enhanced natural convection, while the frustum tube system improved both convection and conduction. Lastly, an insightful review took a comprehensive look at the performance parameters of PCM-MF composites [14]. Many parameters were identified as key influencers, including MF porosity and pore density. Additionally, the review pointed out the heat transfer direction, iteration of thermal cycles, and MF filling ratio as potential areas for further investigation [14].

A dominant theme from the research studies is the amalgamation of PCM with MFs to augment the heat transfer rate in LHTES systems. The rationale behind this synthesis is the high thermal conductivity of MFs, which substantially improves the heat storage efficacy of PCM, thus optimizing the performance of LHTES [15]. However, including MFs can deter the natural convection of PCM, leading to a decline in its LHTES capacity and an escalation in costs [15]. Thus, several configurations of integrating MFs into LHTES systems have recently been investigated. For instance, one study accentuated the shape and placement of the MF layer in determining the efficiency of thermal energy storage [16]. It was discerned that the shape of the MF layer has the potential to modulate the storage power by approximately 60 %, even with a constant amount of MF [16]. Another research, aiming at the composite design of PCM

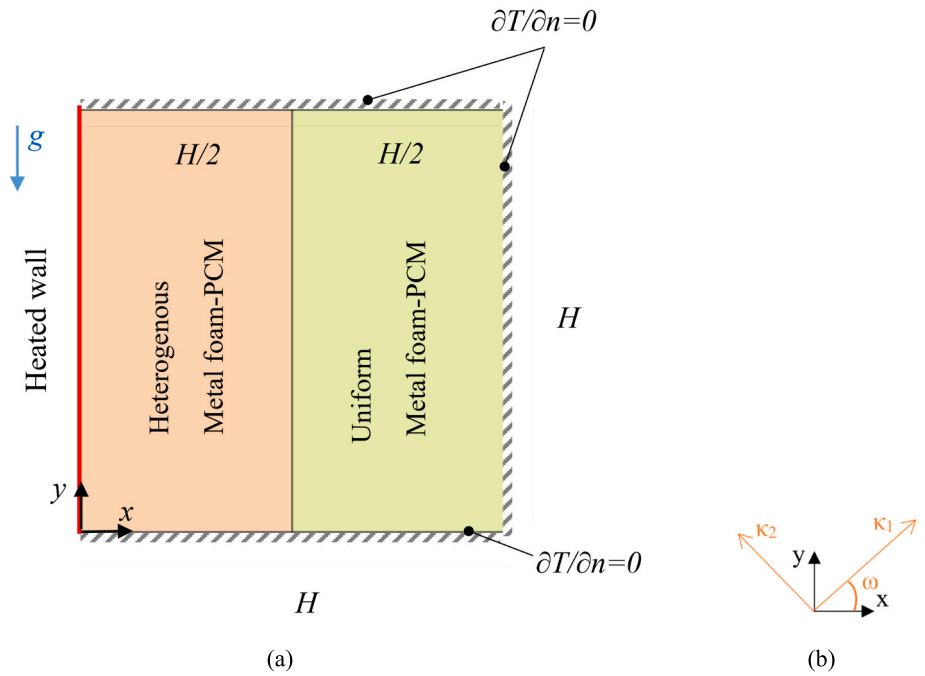

Fig. 2. A detailed view of a PCM channel container filled by two layers of MF. (a) the MF layer configurations, geometrical and boundary conditions; (b) the orthogonal directions of material properties for the heterogeneous MF.

and MF LHTES, evaluated the effects of various factors, such as nanoparticle volumetric fraction and tube wave amplitude, on the unit's performance [17]. It was ascertained that the integration of MFs, coupled with nanoparticles, bolstered heat transmission and curtailed charging time [17]. Progressing with the exploration of configurations, a novel setup for LHTES using a partial filling of MF was proposed [18]. The foundation of this configuration lies in the optimum thermal conductivity enhancer (TCE) density, emphasizing the strategic placement of the MF in regions with high thermal potential [18,19]. Notably, this configuration managed to maintain an equal melting time as that of LHTES with a full volume of MF, demonstrating the potential for reduced system weight and enhanced economic efficiency [18].

Moreover, an in-depth investigation was conducted into the optimal configuration of MF layers using a combination of copper nanoparticles and copper foam [20]. Through applying the Taguchi optimization approach, this research found that when combined with high porosity and nanoparticle volume fraction, specific configurations could trim down the melting time by threefold [20]. Furthermore, empirical studies add significant weight to these claims. One such experimental research focused on a heat sink wherein PCM was embedded in open-cell copper foam [21]. The results indicated that copper foam filled partially with PCM exhibited enhanced thermal performance. Specifically, during the heating process, this configuration showed a temperature drop of 20.1 % compared to the one without any foam or PCM [21]. Further research indicates that incorporating copper foam fins can substantially improve the heat distribution and decrease the time required for melting and solidification processes [22]. In scenarios where the filling ratio is 50 %, optimizing the shapes of copper foam can reduce the complete melting time by 4143 s, significantly increasing the benefit of thermal transfer [23]. Moreover, varying the volume fraction of copper foam has a pronounced effect on thermal behavior, cutting down melting and solidification times by as much as 97.63 % at optimal fractions [24]. Adjusting the porosity and density of the copper foam pores also optimizes thermal performance, with a suggested porosity of 92 % striking a balance between enhancing heat transfer and maintaining storage capacity [25]. The shape of the copper foam fins further influences thermal efficiency, with certain designs promoting better thermal charging and discharging [26]. Additionally, the inclination angle of the cavity partially filled with copper foam affects thermal behavior, with an optimal angle of 180° shortening the phase-change time by 43.16 % [27]. These insights highlight the crucial role of copper foam filling strategies in improving the efficiency of Latent Thermal Energy Storage systems.

Some researchers utilized advanced configurations of MFs, such as several layers of MF with various porosities [28,29], MF with porosity gradients [30,31], or anisotropic MFs [32,33]. A numerical study by Sardari [34] demonstrates the profound influence of porosity, pore density, and the positioning of the heat source on the melting process of PCM in a vertical container embedded with copper MF. The results underscored a significant reduction in melting time by 85 % for the copper foam-PCM unit compared to PCM alone. In addition, strategically altering the heater's location from the base to the side or top could decrease the melting time by 70.5 % and 4.7 %, respectively. Notably, the research also emphasizes the advantage of a multiple-segment MF system, which further reduces the melting time by 3.5 % compared to a uniform porosity system.

Parallel to these findings, a study on a horizontal tank filled with graded MF [35] throws light on the unstable nature of solar energy and the necessity of an effective LTES system. They found that varying porosity gradients can significantly affect the melting rate of PCM, with an optimal combination, reducing the total consumption time by up to 9.7 % and 6.2 % for the melting and solidification processes, respectively. Diving deeper into the intricacies of PCM-MF systems [36] offers insights into the three-dimensional melting heat transfer and the heat storage performance of such a unit. By introducing a gradient porosity across three stratified layers, they aimed to refine the melting characteristics of the composite PCMs. Their findings point to an interesting competitive dynamic between conduction and convection, impacted by the gradient porosity. This balance, in turn, has significant implications for heat transfer and energy storage efficiency.

Further exploring multi-layer PCMs, a study on a triplex heat exchanger employed a three-layer PCM with distinct melting temperatures [37]. The charging speed in the unadulterated three-layer PCM was notably slower than its single-layer counterpart. However, integrating Al-6061 MF amplified the melting rate of the three-layer PCM, enhancing its efficacy. The study [31] underscores the prowess of porous three-layer PCM configurations in thermal energy storage heat

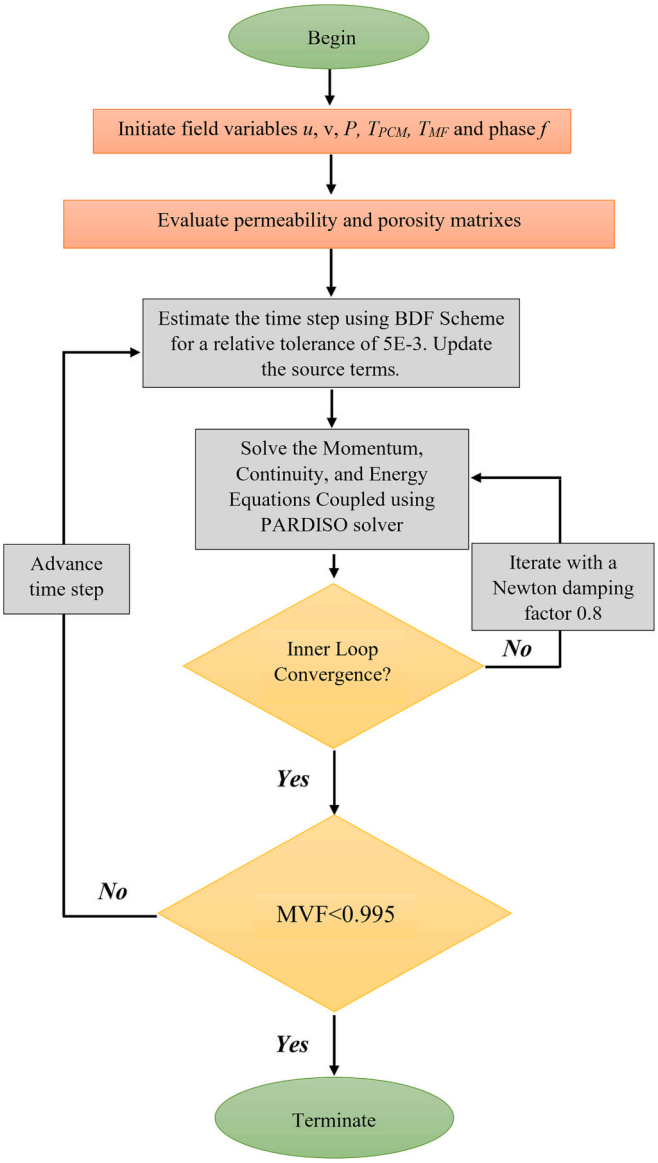

Fig. 3. Schematic representation of the numerical methodology employed to interpret the primary equations.

Table 1
Details of meshes across different mesh control values (*Nm*).

Nm (mesh cases)	Quads	Edge elements	MVF@106 (min)	Err %	Computational time
6	14,641	600	0.999	0.60	20 h:01 min
7	19,881	700	0.991	0.20	22 h:27 min
8	25,921	800	0.991	0.20	25 h:57 min
9	32,761	900	0.992	0.10	30 h:25 min
10	40,000	10,000	0.993	–	37 h:23 min

exchangers. In another study, [38] delved into the augmentation of solidification through a combination of various PCMs, cascading MF, and nanoparticles within a shell-and-tube energy reservoir system. Their findings revealed that the design combining an array of PCMs with layered foam demonstrated superior thermal behavior, registering an impressive 94 % decrement in solidification duration, depending on the count of PCMs and layers of foam used.

As discussed, PCMs combined with MFs have gained substantial attention for their potential in LHTES systems. A pivotal aspect of this research area is the utilization of artificial neural networks (ANNs) and deep neural networks (DNNs) to study and enhance heat transfer mechanisms in thermal systems. The study of Shafi et al. [39] sheds light on the significance of neural networks in predicting phase change heat transfer. The research employs an ANN to model the relation between the nanoparticles fractions and the anisotropic angle, focusing on the melting volume fraction. Their computational model revealed that an ANN could produce highly accurate predictions, evidenced by an R-value close to unity. Furthermore, the study's findings underscore the vital role of MF fins' geometrical placements and the influence of nanoparticle concentrations on heat transfer. Interestingly, while nanoparticles can generally enhance surface heat transfer, they may reduce the thermal storage volume of the heatsink. Another groundbreaking approach came from introducing an Artificial Neural Network (ANN) combined with a Genetic algorithm [40]. Aimed at optimizing the porosity distribution of graded MF, this approach focused on amplifying unidirectional phase-change processes. Their numerical model highlighted the profound effect of graded MF on heat transfer rates, where an optimal distribution could augment heat transfer by a staggering 1160 % and 1185 % for two-layer and three-layer graded MF, respectively.

On a broader note, [41] ventured into the potential of DNNs to understand the physics of 2D heat transfer conduction. Their dataset, which comprised a diverse set of geometries, was introduced to a convolutional DNN. This approach aimed at predicting 2D heat transfer without explicit knowledge of the underlying partial differential equation. The study introduced two novel loss functions tailored for heat transfer physics. Results indicate the robust capability of DNNs in comprehending physical problems and suggest one of the loss functions as a potentially superior training tool. In a parallel stride, [42] further delves into the efficacy of loss functions in the deep learning paradigm. The research introduces three novel loss functions to bolster the training of DNNs for thermal conduction problems. Their findings highlight that one of these new loss functions significantly outperforms conventional ones, improving prediction accuracy and minimizing errors.

Deep learning's versatility is further illustrated in [43], which employs a DNN for parameter classification in natural convection heat transfer of nano-encapsulated PCM. By leveraging isotherm images, the DNN could accurately classify the effects of the Rayleigh number and nanoparticle volume concentrations. Additionally, a transfer learning approach significantly enhanced the accuracy of Stefan number classification. Lastly, [44] extends the application of ANNs to study phase change processes in an inclined container filled with PCM and an MF-fin hybrid structure. Results suggest that combining MF and fins can significantly reduce melting time, especially with an increased number of fins. The ANNs used in the study demonstrated excellent predictions of various heat transfer metrics, affirming their role in such applications.

The literature review underscores the significance of designing LHTES units with advanced heat transfer attributes in renewable energy systems. Notably, more research is needed to enhance the heat transfer of LHTES units using MF layers, especially innovative heterogeneous MFs. This research explores the thermal storage and heat transfer of LHTES units amplified by uniform and heterogeneous MF layers. Additionally, artificial neural networks are employed to understand the system's thermal dynamics and refine the unit design.

2. Model description

Fig. 1 illustrates a schematic view of an LHTES unit made of heat transfer fluid (HTF) passages and channel-shaped containers filled by PCMs. The HTF fluid is water, which passes over the PCM container walls. One side of each PCM container is in contact with the HTF, exchanging heat to water at a temperature T_h, and melts the PCM at a fusion temperature T_m while ($T_m < T_h$). The melting phase change of PCM absorbs a notable amount of energy, which can be later released in a solidification process.

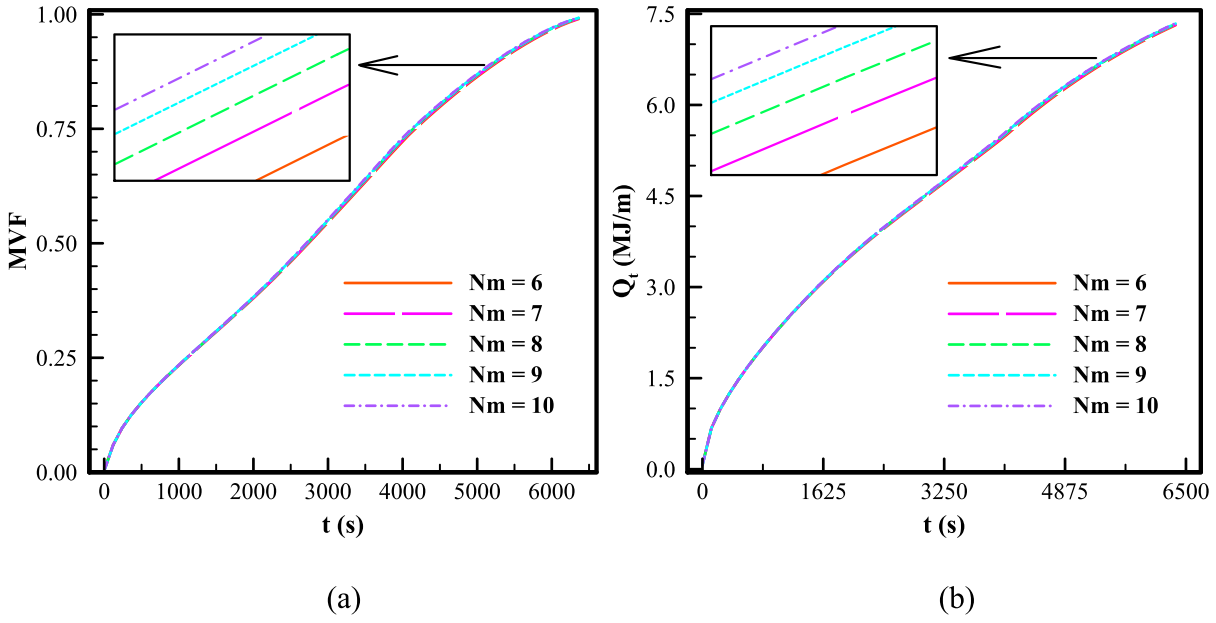

Fig. 4. How the mesh resolution parameter (*Nm*) influences (a) the melting progression and (b) the stored energy.

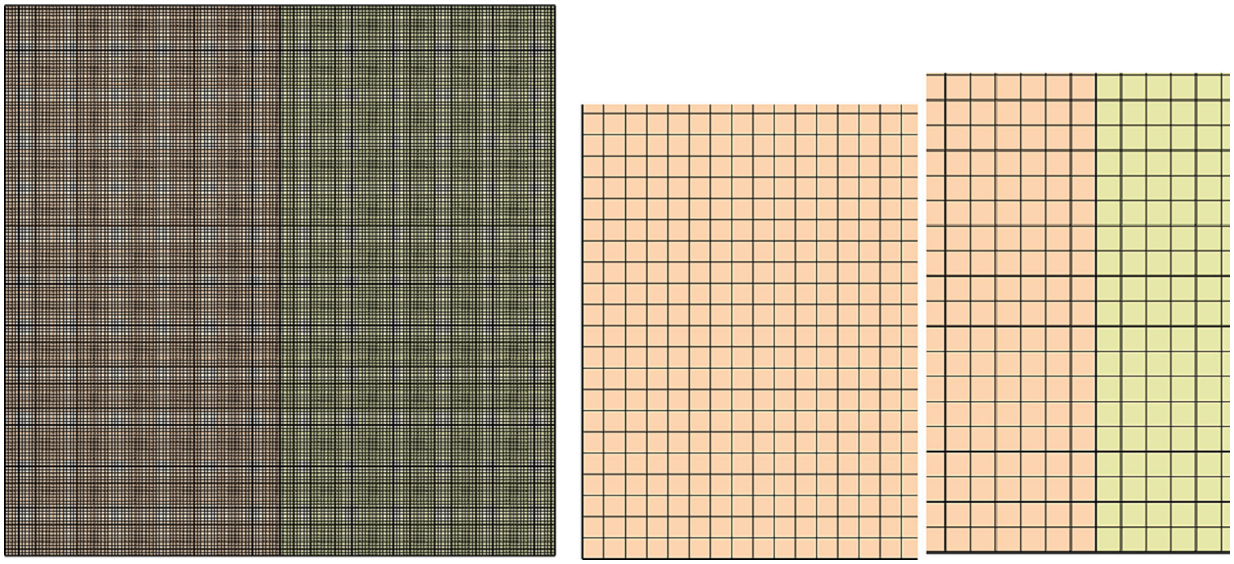

Fig. 5. Comprehensive and close-up perspectives of the mesh at $Nm = 8$.

Two layers of MF are utilized to improve heat transfer in the PCM containers. A detailed view of the channel section is depicted in Fig. 2. The first MF layer comprises a heterogeneous MF with engineered local properties, while the second layer is a uniform MF. The permeability and thermal conductivity of the heterogeneous MF depend on an anisotropic parameter (K_n) and anisotropic angle (ω). The heterogeneous properties can be controlled by adding material to one direction and removing it from another direction. Some anisotropic metal foams are discussed in [45–47]. *Kn* can be considered as the ratio of the excess material in a perpendicular direction compared to the average material. Thus, the MF's thermal conductivity (k) and permeability (κ) of the heterogeneous MF are introduced as [48]:

$$k_{\mathrm{MF}} = \begin{bmatrix} k_1(cos\omega)^2 + k_2(sin\omega)^2 & (k_1 - k_2)(sin\omega)(cos\omega) \\ (k_1 - k_2)(sin\omega)(cos\omega) & k_1(sin\omega)^2 + k_2(cos\omega)^2 \end{bmatrix} \quad (1)$$

$$\kappa = \begin{bmatrix} \kappa_1(cos\omega)^2 + \kappa_2(sin\omega)^2 & (\kappa_1 - \kappa_2)(cos\omega)(sin\omega) \\ (\kappa_1 - \kappa_2)(cos\omega)(sin\omega) & \kappa_1(sin\omega)^2 + \kappa_2(cos\omega)^2 \end{bmatrix} \quad (2)$$

where subscript MF indicates the metal foam and subscripts 1 and 2 are the orthogonal directions, as introduced in Fig. 2. Besides, $k_2 = (1-K_n) \times k_m$, $k_1 = (1 + K_n) \times k_m$, and $\kappa_2 = (1 + K_n) \times \kappa_m$, $\kappa_1 = (1\text{-}\sigma) \times \kappa_m$ [32,49]. k_m and κ_m are the average properties of a simple metal foam. The MF's average property is represented by the subscript *m*. More details about computing thermophysical properties related to anisotropic aspects such as κ_m and k_m can be found in [32].

2.1. Governing equations

The heat transfer and phase change of PCM inside the MF layer and the natural convection circulation of liquid PCM inside the MF pores can

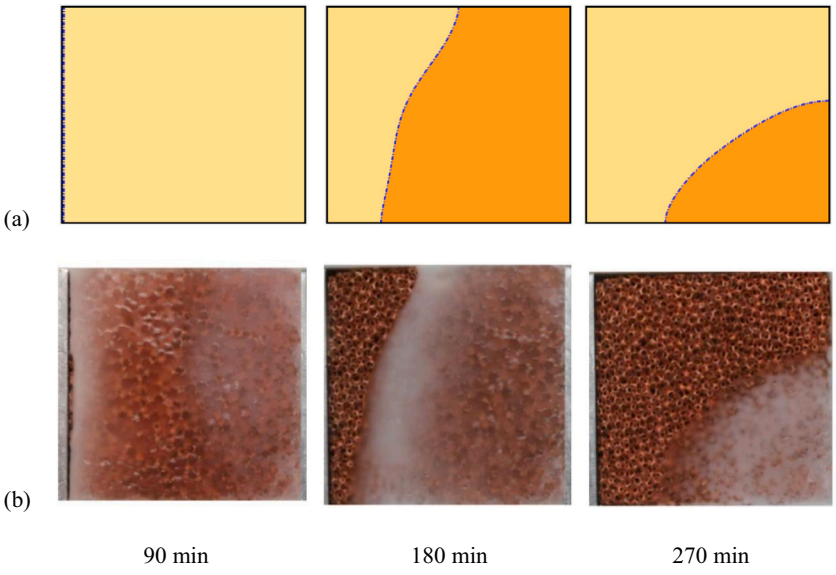

Fig. 6. Melting patterns of hybrid PCM-MF paraffin wax within a square chamber: (a) results from our recent study and (b) hands-on data from [63] (with permission from Elsevier).

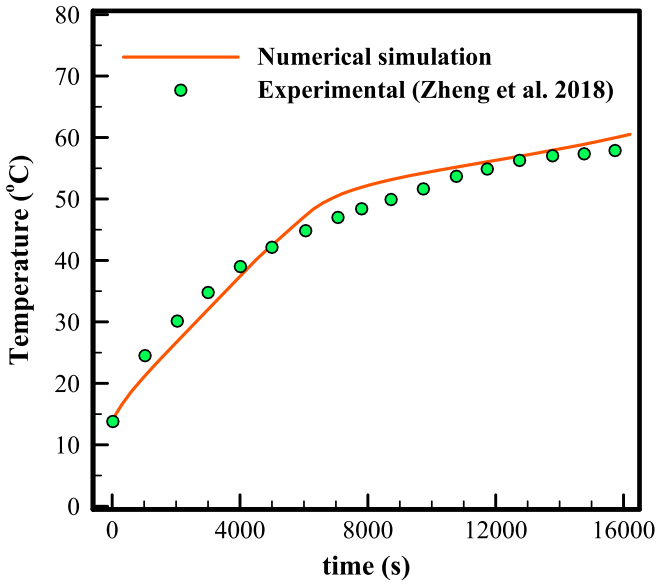

Fig. 7. Verification of current study through comparison with empirical [63] measurements.

be explained by physical laws of conservation of mass, momentum, and energy. The following provides partial differential equations representing the physical behavior of a channel PCM during a melting process. The model for fluid flow in the metal foam is based on the Darcy-Brinkman-Forchheimer framework [17,50,51]:

Conservation of mass:

$$\frac{\partial u}{\partial x}+\frac{\partial v}{\partial y}=0 \tag{3}$$

The x-momentum equation:

$$\frac{\rho_{\mathrm{PCM}}}{\varepsilon}\frac{\partial u}{\partial t}+\frac{\rho_{\mathrm{PCM}}}{\varepsilon^2}\left(u\frac{\partial u}{\partial x}+v\frac{\partial u}{\partial y}\right)=-\left(\frac{\partial p}{\partial x}\right)+\frac{1}{\varepsilon}\left[\frac{\partial}{\partial x}\left(\mu_{\mathrm{PCM}}\frac{\partial u}{\partial x}\right)+\frac{\partial}{\partial y}\left(\mu_{\mathrm{PCM}}\frac{\partial u}{\partial y}\right)\right]$$
$$-\frac{\mu_{\mathrm{PCM}}}{\kappa}u-\rho_{\mathrm{PCM}}\frac{C_F}{\sqrt{\kappa}}|U|u+A_{mush}\frac{(1-f(T))^2}{\lambda_{mush}+f^3(T)}u \tag{4}$$

The y-momentum equation in y direction:

$$\frac{\rho_{\mathrm{PCM}}}{\varepsilon}\frac{\partial v}{\partial t}+\frac{\rho_{\mathrm{PCM}}}{\varepsilon^2}\left(u\frac{\partial v}{\partial x}+v\frac{\partial v}{\partial y}\right)=-\left(\frac{\partial p}{\partial y}\right)+\frac{1}{\varepsilon}\left[\frac{\partial}{\partial x}\left(\mu_{\mathrm{PCM}}\frac{\partial v}{\partial x}\right)+\frac{\partial}{\partial y}\left(\mu_{\mathrm{PCM}}\frac{\partial v}{\partial y}\right)\right]$$
$$+g\rho_{\mathrm{PCM}}\beta_{\mathrm{PCM}}(T-T_0)-\frac{\mu_{\mathrm{PCM}}}{\kappa}v-\rho_{\mathrm{PCM}}\frac{C_F}{\sqrt{\kappa}}|U|v+A_{mush}\frac{(1-f(T))^2}{\lambda_{mush}+f^3(T)}v \tag{5}$$

The conservation of energy in PCM:

$$\varepsilon(\rho C_p)_{\mathrm{PCM}}\frac{\partial T_{\mathrm{PCM}}}{\partial t}+(\rho C_p)_{\mathrm{PCM}}\left(u\frac{\partial T_{\mathrm{PCM}}}{\partial x}+v\frac{\partial T_{\mathrm{PCM}}}{\partial y}\right)=$$
$$\frac{\partial}{\partial x}\left(k_{\mathrm{eff,PCM}}\frac{\partial T_{\mathrm{PCM}}}{\partial x}\right)+\frac{\partial}{\partial y}\left(k_{\mathrm{eff,PCM}}\frac{\partial T_{\mathrm{PCM}}}{\partial y}\right)+h_v(T_{\mathrm{MF}}-T_{\mathrm{PCM}})-\varepsilon\rho_{\mathrm{PCM}}L_{\mathrm{PCM}}\frac{\partial f(T)}{\partial t} \tag{6}$$

The conservation of energy in MF:

$$(1-\varepsilon)(\rho C_p)_{\mathrm{MF}}\frac{\partial T_{\mathrm{MF}}}{\partial t}=\frac{\partial}{\partial x}\left(k_{\mathrm{eff,MF}}\frac{\partial T_{\mathrm{MF}}}{\partial x}\right)+\frac{\partial}{\partial y}\left(k_{\mathrm{eff,MF}}\frac{\partial T_{\mathrm{MF}}}{\partial y}\right)-h_v(T_{\mathrm{MF}}-T_{\mathrm{PCM}}) \tag{7}$$

Here, a detailed local thermal none-equilibrium (LTNE) model is utilized to take into account the temperatures of solid MF and PCM inside the MF pores. The density, thermal conductivity, and specific heat capacity are denoted by ρ, k, and Cp, respectively. T symbolizes the temperature field, while t stands for time. The pressure (p), x, and y velocity components (u and v) denote the hydraulic field variables. The heat transfer between MF and PCM in the volumetric unit was represented in the energy Eqs. (6) and (7) through the coefficient h_v [52]. The given equations make use of the acceleration due to gravity (g), the coefficient related to thermal volume expansion (β), the parameter known as the Frochheimer factor (C_F), and the latent heat associated with fusion (L). The values of $A_{\mathrm{mush}} = 10^{10}$ Pa.s/m^2 and $\lambda_{\mathrm{mush}} = 10^{-3}$ were applied to control the domain's PCM velocity. $|U|$ is the effective

velocity$|U| = \sqrt{u^2+v^2}$. Subscript PCM denotes the PCM material, and f is the phase change field introduced as [53]:

$$f(T) = \begin{cases} 0 & T < Tm - \frac{1}{2}\Delta Tm \,(\text{Solid PCM}) \\ \frac{(T-Tm)}{\Delta Tm} + \frac{1}{2} & Tm - \frac{1}{2}\Delta Tm \le T \le Tm + \frac{1}{2}\Delta Tm \,(\text{Solid} - \text{Liquid PCM region}) \\ 1 & T > Tm + \frac{1}{2}\Delta Tm \,(\text{Liquid PCM}) \end{cases} \quad (8)$$

Also, further information about the LTNE properties is available in [52]. The thermophysical properties of Copper (MF) [33] and paraffin wax (PCM) were taken from the literature [54–56]. The fusion temperature of PCM was considered as the average temperature of solid-liquid temperatures as $Tm = 51.5$ °C. The enclosure size (H) was set as 15 cm in the current study.

2.2. Boundary and initial conditions

The non-slip and impermeability conditions were applied for all enclosure surfaces. A reference pressure with zero value was used at the top-left corner of the enclosure. The left wall of the channel, as depicted in Fig. 2, is at a hot temperature of $Th = (Tm + 15$ °C) while the remaining surfaces are well insulated. The PCM and MF in the enclosure are initially at a supper cold temperature $T_0 = (Tm\text{-}15$ °C). The reported temperatures are the temperature differences defined as $\Delta T = T\text{-}T_0$ (°C).

2.3. Characteristic parameters

The melting volume fraction represents the mean amount of PCM that has melted, and its determination can be achieved through the provided equation:

$$MVF = \frac{\oint_v f \epsilon dV}{\oint_V \epsilon dV} \quad (9)$$

Wherein dV stands for the volume element within the shell domain.

To compute the total thermal energy retained, both the latent and sensible heat are combined:

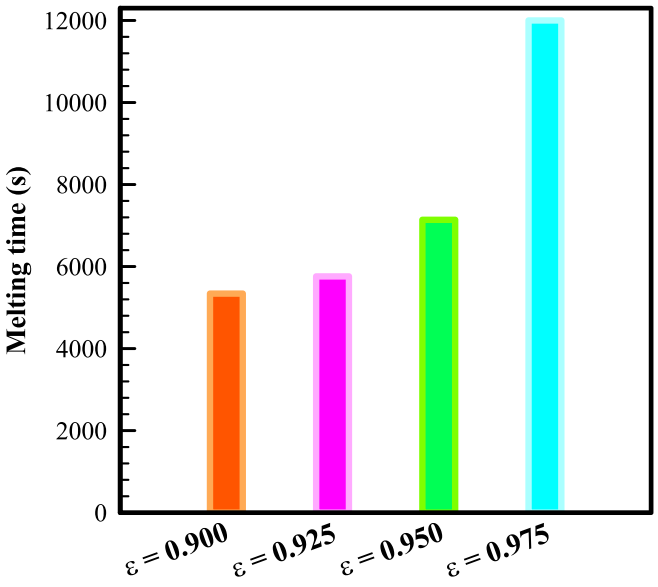

Fig. 9. A graphical representation of melting times when MVF = 0.95 for various values of porosity.

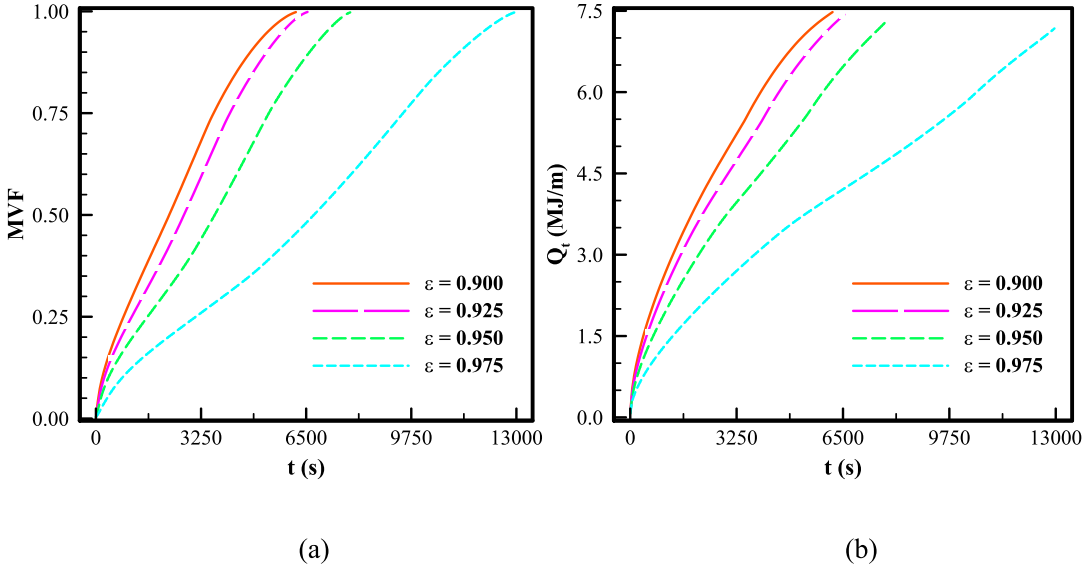

Fig. 8. The influence of porosity (ε) on the time history of: (a) MVF and (b) stored energy.

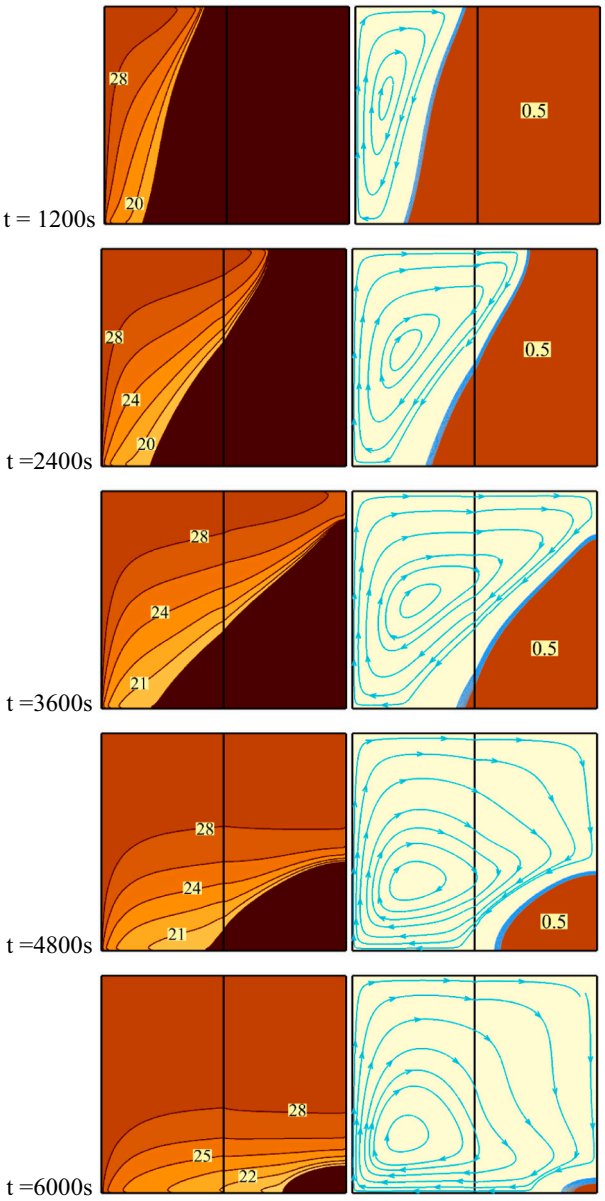

Fig. 10. The isotherms (ΔT), melting interface, and streamlines at $\varepsilon = 0.9$ for various melting times.

$$Q = \{(\rho C_P)_{\mathrm{MF}} \oint_V (1-\varepsilon)dV\}(T - T_0) + \left[\oint_V \left(\varepsilon \int_{T_0}^{T} (\rho C_P)_{\mathrm{PCM}} dT\right) dV\right] + \varepsilon \oint_V f \rho_{\mathrm{PCM}} L_{\mathrm{PCM}} dV \quad (10)$$

To measure the rate of energy storage, one divides the accumulated energy by the elapsed time:

$$P = Q/time \quad (11)$$

The rate at which thermal energy is stored signifies the energy accumulated from the cold PCM's initial state up to a distinct point during the charging phase.

In the present study, Kn = 0.3 was adopted for the heterogenous foam layer parameter. The heterogeneous angle was investigated in the $0 < \omega < 90^{\circ}$ range, and average porosity in the $0.9 < \varepsilon < 0.975$ range. Base values of $\omega = 0.785$ rad (45°), $\varepsilon = 0.925$, and $Kn = 0.3$ were adopted for the presentation of the results. Otherwise, the value will be stated.

3. Solution approach and model verification

This section provides the quantitative technique, model evaluations, and mesh sensitivity scrutiny.

3.1. Utilization of the Finite Element Technique (FET)

To decipher the core equations, along with their boundary and initial conditions, the Finite Element Technique (FET) was employed. This method was essential for efficiently handling the nonlinear sink/source elements associated with phase transformation [57,58]. The governing partial differential equations are transformed into a weak form. A second order discretization for momentum and thermal equations was utilized. The set of equations were integrated via the Gauss quadrature integration on an element-by-element basis to find algebraic residual equations. Iterative solutions for these equations were found using the Newton technique [59,60], and a damping coefficient of 0.8 was incorporated to enhance the convergence rate. In collaboration with the Newton approach, the PARDISO parallel computation system was deployed to facilitate simultaneous calculations across multiple processing units [61,62].

Autonomously, the solution's timing and convergence were adjusted to maintain a relative error under 5×10^{-3}, utilizing the backward differential formula's primary-secondary order. The FET ensures a smooth and precise outcome over the segmented mesh, aligning perfectly with the goals of this research. Initiating with the starting conditions, the study progressed to investigate phase transition dynamics and energy storage. Equations relating to thermal aspects, continuity, and the phase change field (f) were deemed fully consolidated and solved in a step-by-step manner. The algorithm was designed to be terminated when an utterly molten state was reached, recognized by an MVF value greater than or equal to 0.995, serving as the completion metric. A schematic representation of the applied computational approach can be observed in Fig. 3.

3.2. Mesh sensitivity analysis

To analyze the effect of mesh resolution on computational accuracy, a test case with $Kn = 0.3$, $\omega = 45^{\circ}$, and $\varepsilon = 0.925$ was examined. The domain of the solution was partitioned using a uniform structured mesh. *Nm*, a mesh resolution parameter, was used to dictate the size of the mesh. Table 1 showcases the attributes of the generated meshes, the MVF at $t = 106$ min, and the associated computational durations. This particular time frame of 106 min was chosen due to its proximity to the complete melting phase.

As seen in Table 1, there is a clear inverse relationship between the mesh resolution parameter, *Nm*, and the associated error percentage, Err %. As *Nm* increases from 6 to 9, the error consistently decreases, moving from 0.60 % at $Nm = 6$ to just 0.10 % at $Nm = 9$. This trend highlights that a finer mesh resolution typically results in more accurate computational representations. The impact of mesh resolution parameter on the melting fraction and stored energy is plotted in Fig. 4 during the energy storage process.

As the mesh resolution parameter, *Nm,* ascends from 6 to 10, there is an evident and direct relationship with the computational time: from 20 h:01 min at $Nm = 6$ to 37 h:23 min at $Nm = 10$. Interestingly, the increase in computational time does not just grow, but the gaps between consecutive *Nm* values expand, hinting at a potentially exponential rise in computational demands with mesh refinement. This trend mirrors the inverse relationship observed between *Nm* and the error percentage (Err %), where higher mesh resolutions led to reduced errors. This correlation between *Nm*, computational time, and Err % illuminates a pivotal trade-off in computational modeling. As mesh granularity intensifies, while accuracy gains are achieved (as evidenced by lower Err %), they

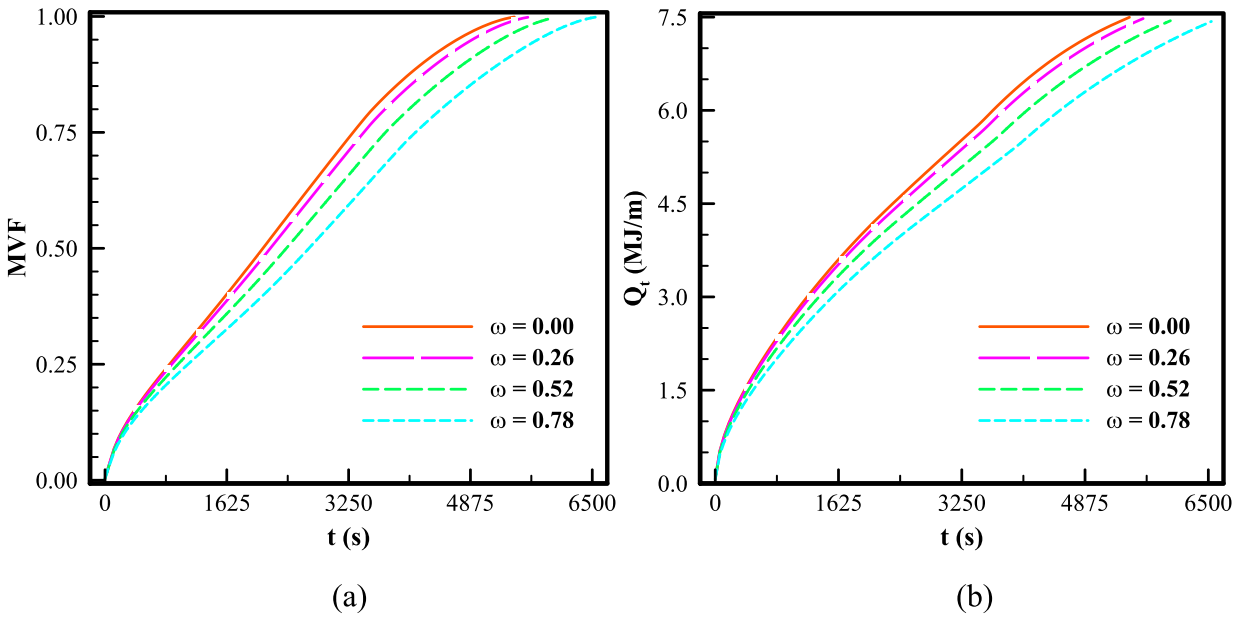

Fig. 11. The influence of heterogeneous angle ω (rad) on time history of: (a) MVF and (b) stored energy.

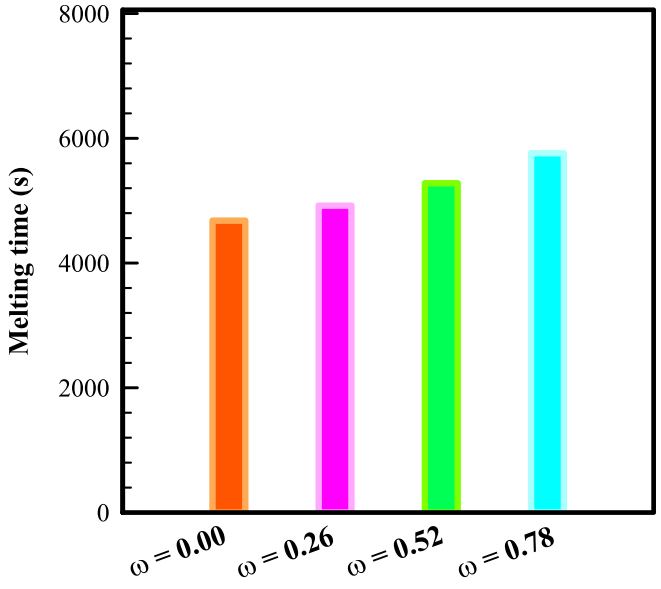

Fig. 12. A graphical representation of melting times when MVF = 0.95 for various values of heterogeneous angles ω (rad).

come at the high cost of extended computational durations. Thus, as a fair trade between computational time and accuracy, Mesh with $Nm = 8$ was selected. The structure of mesh with Nm=4 is depicted in Fig. 5.

3.3. Model verification

During the melting procedure of the hybrid PCM-MF paraffin wax, the results generated by our simulations were compared to experimental observations shared by Zheng et al. in [63]. Within a square enclosure of 100 mm, paraffin wax underwent the melting phase. A heat flux of 1150 W was administered to a singular vertical face, with only slight heat loss from the surrounding boundaries of the compartment. The metal foam made of copper had a porosity of 0.95 and a PPI of 5. Fig. 6 showcases the liquid-solid boundary at intervals of 90 min, 180 min, and 270 min during the melt. Meanwhile, Fig. 7 visualizes the average temperature along a vertical trajectory situated 2.5 cm from the warmth-infused plane. The present simulation's observed structure, boundary points, and temperature outlines resonate strongly with the observations made by Zheng et al. [63].

4. Results and discussion

Fig. 8 presents the chronological progression of MVF and stored energy throughout the melting process. A notable observation is that an increase in porosity considerably prolongs the melting process. To illustrate, let's consider a scenario where the MVF is 0.5, signifying that half the enclosure is filled with molten PCM. For cases with porosities $\varepsilon = 0.9$, $\varepsilon = 0.925$, $\varepsilon = 0.95$, and $\varepsilon = 0.975$, the respective melting durations are 2280 s, 2760 s, 3720 s, and 6780 s. Interestingly, a modest porosity increase of 7.5 % from 0.9 to 0.975 augments the melting duration by a striking 66 %. This underscores the profound influence of the average porosity of the MF layers on heat transfer and energy storage rates. For an MVF of 0.5, Fig. 8(b) reveals that the energy storage rates for $\varepsilon = 0.9$ and $\varepsilon = 0.975$ are 1848 W and 637 W, respectively. This implies that a 7.5 % augmented use of metal foam (at $\varepsilon = 0.9$), enhances the thermal properties and then, amplifies the power rate by almost 2.9 times when juxtaposed with the $\varepsilon = 0.975$ scenario. The unit of MJ/m was employed as the unit for energy storage, assuming a unit length of unity.

Fig. 9 graphically elucidates the melting times required for MVF = 0.95. A conspicuous disparity is observed between the $\varepsilon = 0.95$ and $\varepsilon = 0.975$ cases, while the differences among other cases appear relatively nominal. This suggests that selecting a metal foam with an average porosity of 0.95 or 0.925 might strike an optimal balance between enhanced heat transfer and minimal material addition. As the porosity is reduced to 0.9, the amount of metal foam matrix increases, but the heat transfer enhances slightly. The fastest melting occurs in the scenario with $\varepsilon = 0.9$, which intriguingly also shows the greatest resistance to natural convection currents. Therefore, the $\varepsilon = 0.9$ scenario has been selected for an in-depth analysis of temperature distribution and patterns of melting.

Fig. 10 offers insights into the isotherms and the melting frontier, supplemented by streamlines for the $\varepsilon = 0.9$ case, captured at intervals beginning from 1200s. At the 1200s mark, the melting boundary predominantly progresses at the enclosure's upper section, attributable to the influences of natural convection. The molten regions feature

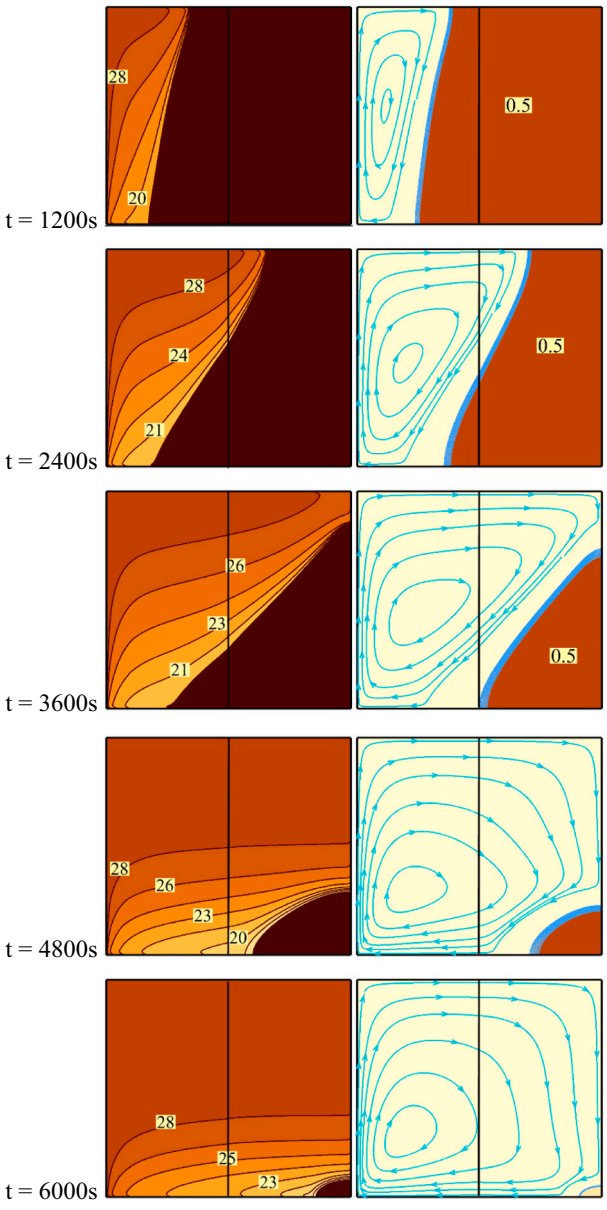

Fig. 13. The isotherms (ΔT) and streamlines at $\omega = 0$ rad for various melting times.

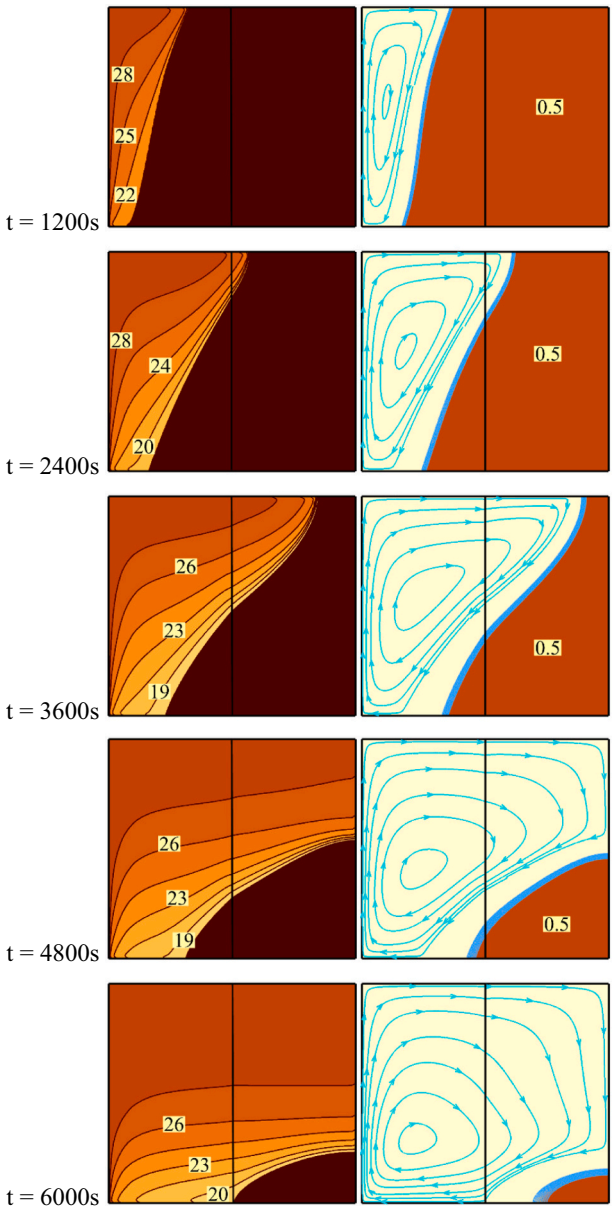

Fig. 14. The isotherms (ΔT) and streamlines at $\omega = 0.785$ rad (90°) for various melting times.

prominently developed streamlines, indicating fluid movement ascending adjacent to the heated surface, reaching the melting boundary, relinquishing heat to the solid PCM, and then descending. With the progression of time, melting continues, notably shrinking the solid region to the right. Close-knit isotherms, especially at the enclosure's upper section, indicate pronounced temperature gradients. By the 6000 s mark, the enclosure predominantly transitions to a liquid state, with temperatures approximating the heated wall's temperature. At the same time, the gaps in the streamlines become smaller, indicating a decrease in natural convection as a result of lessened temperature differences and weaker buoyancy forces.

Fig. 11 presents the melting fraction and stored energy across varying heterogeneous angles: $\omega = 0$ rad (0°), 0.26 rad (30°), 0.52 rad (60°), and 0.78 rad (90°). Augmenting the heterogeneous angle results in a lag in both the melting process and stored energy.

Fig. 12 sheds light on the melting duration corresponding to each heterogeneous angle. The least duration is associated with the zero heterogeneous angle. This unique pattern can be attributed to the anisotropic characteristics of the MF layer. When $\omega = 0$, in line with the heterogeneous matrices defined by Eqs. (1) and (2), there's a notable enhancement in thermal conductivity in the x-direction coupled with increased permeability in the y-direction. This dual mechanism facilitates the MF layer in effectively absorbing heat from the hot wall primarily through conduction. The heightened permeability in the y-direction then bolsters natural convection flows, ensuring optimal natural convection circulations. As a result, these circulations efficiently spread the absorbed heat in the y-direction through the process of advection, thereby enhancing heat distribution. On the other hand, an angle of 90° demonstrates weaker conduction heat transfer perpendicular to the hot surface while also resisting natural convection flows adjacent to the heated surface. Both these factors collectively hinder convection heat transfer. Melting typically initiates adjacent to the hot wall, extending toward the enclosure's center.

Fig. 13 shows isotherms and streamline contours and the melting front for the anisotropic angle $\omega = 0°$. Comparing with similar contours in Fig. 10 for $\omega = 45°$, we observe that the top region in Fig. 10 exhibits advanced melting for $t = 1200$s. This can be linked to superior thermal

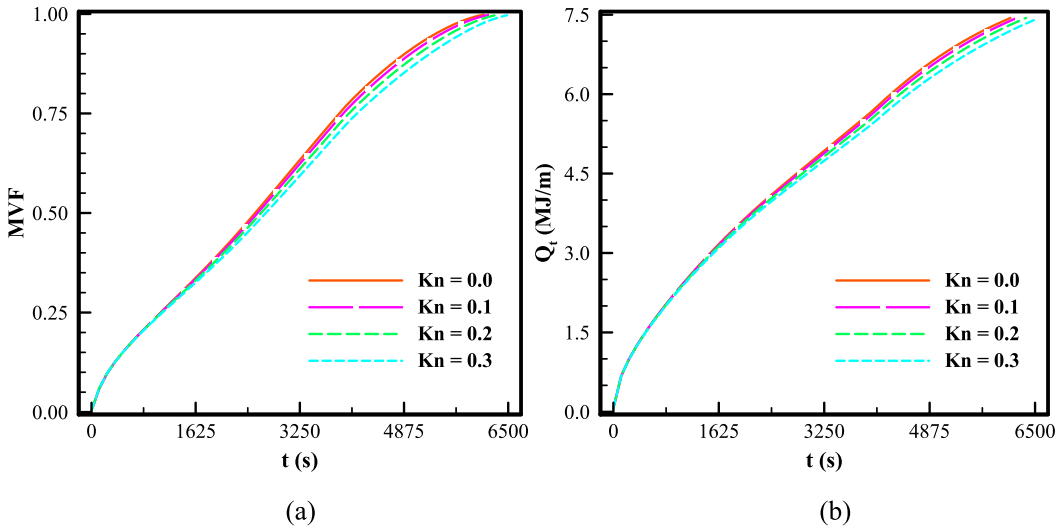

Fig. 15. The influence of heterogeneous parameter (*Kn*) on time history of: (a) MVF and (b) stored energy.

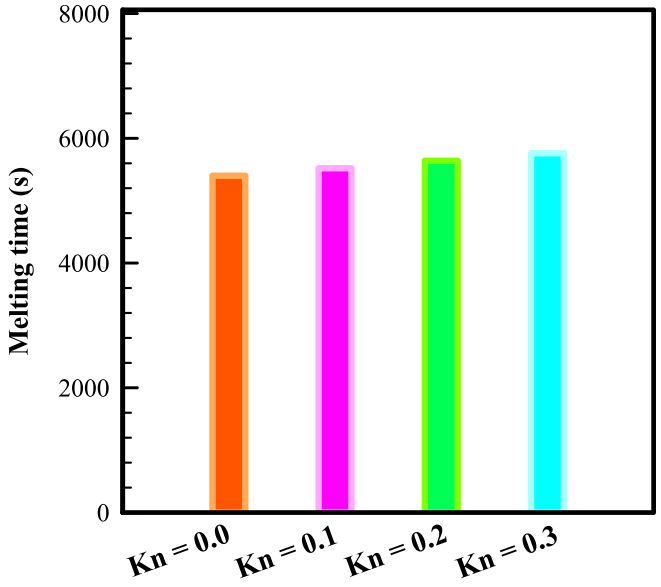

Fig. 16. The required time for the melting process and the total heat released for various ε, ω, and *Kn* for MVF = 0.95 (95 %).

conductivity in the MF layer for $\omega = 0°$ in the x-direction. Additionally, during the early stages (at $t = 1200$s), only a small quantity of PCM is available, indicating a weak natural convection flow. A closer look at Fig. 11 also indicates minimal discrepancies between melting curves in the early stages as ω varies. By $t = 2400$ s, the natural convection dynamics intensify, pushing the melting boundary rapidly upwards. Fig. 14 shows the same contours but for $\omega = 90°$. As seen, the melting interface is not as advanced as that of Fig. 13 at $t = 2400$, which is due to the low permeability of the MF layer with $\omega = 90°$ in the y direction. For both cases of $\omega = 0°$ and $\omega = 90°$, melting also progresses commendably at the base. By $t = 4800$ s, the bulk of the PCM has transitioned to a molten state, and a stratified zone is evident in the enclosure's upper section. However, it is clear that the amount of solid PCM is much higher in Fig. 14 for case $\omega = 90°$. Yet, in both cases, consistent natural convection currents persist in the lower section. By $t = 6000$ s, the entirety of the enclosure nearly matches the wall temperature, with no residual solid PCM.

Fig. 15 illustrates the effects of the heterogeneous parameter, *Kn*, on MVF and stored energy, with results detailed for a default angle of $\omega = 45°$. Notably, the influence of *Kn* on both MVF and stored energy appears to be marginal. Most disparities emerge during the concluding phases of the melting process when only a trace amount of solid PCM remains, and there is a shift in streamline patterns. Additionally, for this particular scenario, the presence of a heterogeneous structure might slightly hamper the melting process. This can be ascribed to the chosen angle $\omega = 45°$, which not only diminishes permeability in the y-direction but also results in reduced thermal conductivity in the x-direction.

Fig. 16 depicts the melting durations. Observably, variations in *Kn* exert a negligible effect on the melting timeframe. Figs. 17 and 18, which display the isotherms, reveal only minor thermal and melting discrepancies between the $Kn = 0$ and $Kn = 0.3$ scenarios. This minimal variation can be attributed to the angle $\omega = 45°$, which furnishes balanced local properties in both the x and y directions, effectively neutralizing each other's impacts.

5. Neural network-based exploration on heat transfer analysis

The computations of phase change heat transfer are pretty expensive. The results of the Mesh sensitivity analysis in Section 3.2 showed that the computational time for the selected mesh case of $Nm = 8$ is about 26 h. Therefore, here in order to better understand the behavior of physical systems for a range of design parameters, the neural networks have been leveraged to dive deeper into the influence of control parameters on heat transfer rates. This specific network is structured with three interconnected hidden layers. Each of these layers holds 15 neurons, utilizing sigmoid as their activation function, as shown in Fig. 19. A dataset spanned 36 distinct melting cases providing 7838 samples was created using the simulated data. The dataset details a myriad of parameters elaborated within the results section. Inputs and outputs processed by the neural network are listed in Table 2. The range of each input parameter is also reported in the table.

The data were normalized in the range -1 to 1, and the dataset was randomized before the training process began, allocating 70 % for training and evenly splitting the remainder for both validation and testing purposes. During the training process, the objective was to reduce the Mean Squared Error (MSE) by employing the Adam optimizer [64]. The neural network was exposed to 1000 training episodes with batch sets of 4. To streamline the data, the StandardScaler methodology [65] was employed. The validation and training and loss values achieved were both below 9×10^{-4}.

Fig. 20 depicts the MSE's trajectory for the training and validation datasets across various epochs, signifying a continuous decline with increasing epochs. Meanwhile, Fig. 21 juxtaposes the actual versus the

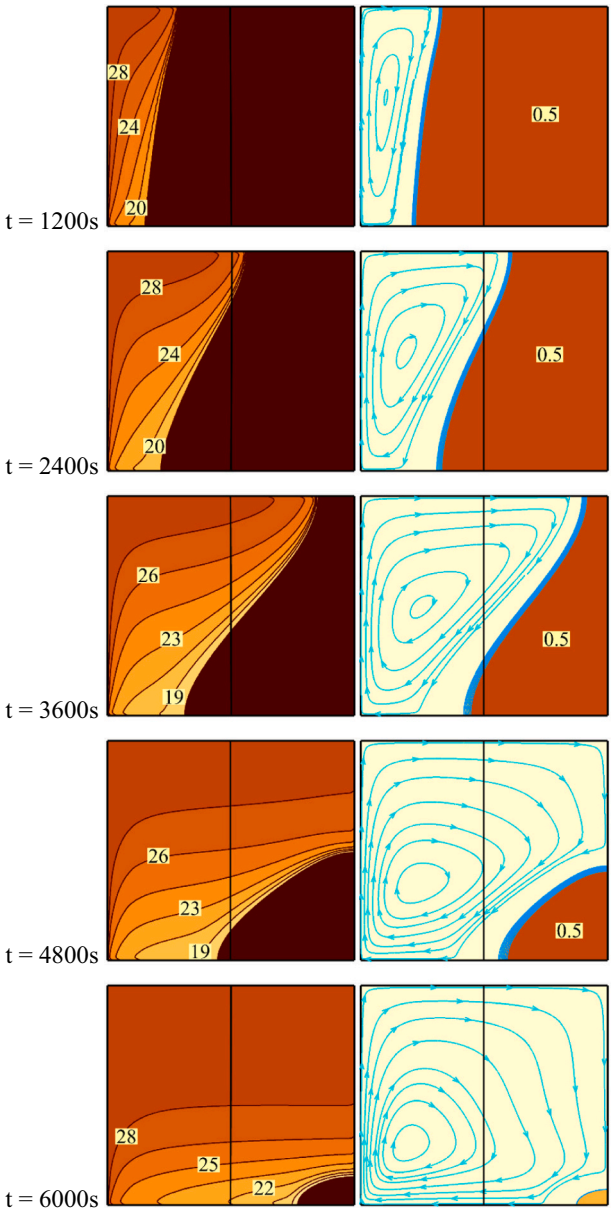

Fig. 17. The isotherms (ΔT) and streamlines at $Kn = 0$ for various melting times.

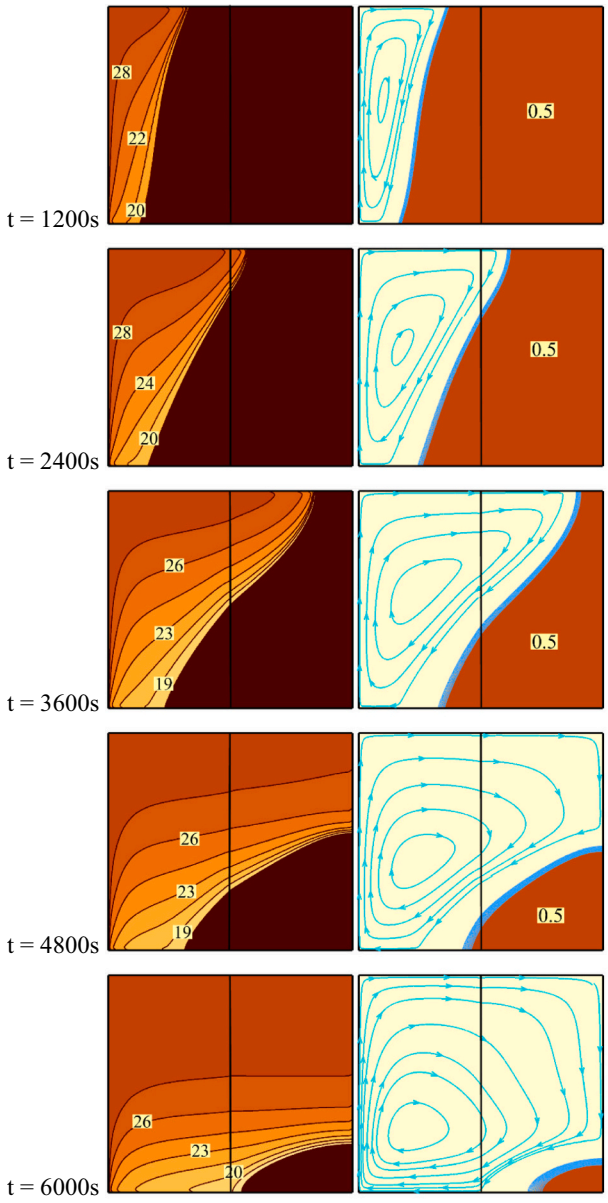

Fig. 18. The isotherms (ΔT) and streamlines at $Kn = 0.3$ for various melting times.

projected test data, evidencing a robust model alignment. Leveraging this neural network's precise predictive capabilities, contour diagrams were drawn to elucidate the influence of the control parameters on MVF.

Fig. 22(a) and (b) present contour plots of *MVF* in relation to *Kn* and ω, captured at time intervals of $t = 2000$ s and $t = 3000$ s with ε set at 0.9. These contours offer insights into heat transfer velocities across various control parameters. Achieving such detailed results was computationally intensive before the adoption of ANNs. In the absence of ANNs, generating this level of detail would have demanded thousands of computational hours. A key takeaway from Fig. 22(a) and (b) is the positive correlation between an increase in the heterogeneous parameter (*Kn*) and the melting rate (*MVF*), especially as the anisotropic angle (ω) diminishes. This trend aligns with the findings from the prior sections regarding the parametric analysis. Furthermore, Fig. 22(a) and (b) shed light on the effects of the anisotropic angle, highlighting that for angles of $\omega > 45°$, a rise in *Kn* can actually reduce *MVF* rather than enhance it.

Fig. 23(a) and (b) showcase MVF corresponding to different

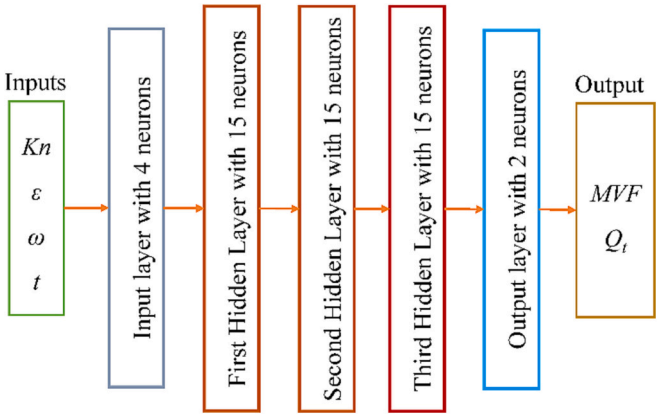

Fig. 19. The structure of utilized NNs for learning the physical dynamic of the energy storage unit.

Table 2
List of input and outputs of ANNs.

Input parameters		Range
Symbol	Description	
K_n	Heterogenous parameter	$0 < K_n < 0.3$
ε	Average porosity	$0.9 < \varepsilon < 0.975$
ω	Anisotropic angle in metal foam (°)	$0 < \omega < 90°$
t	Physical time (s)	$0 < t < 17{,}000$
Output parameters		
MVF	Melting volume fraction	$0 < MVF < 1$
Q_t	Stored energy (MJ)	$0 < Q_t < 7.5$

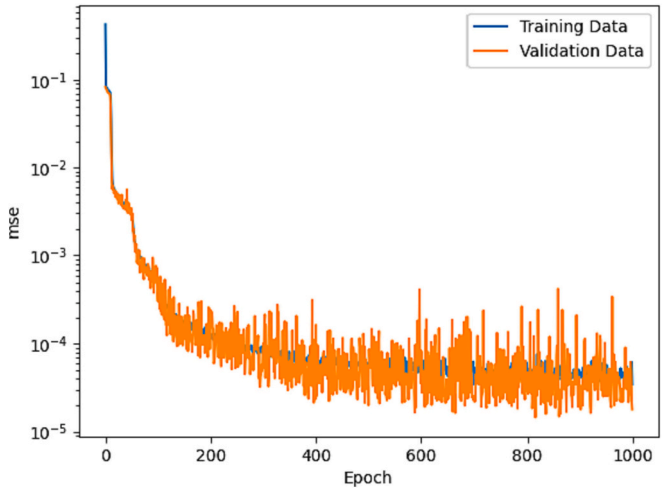

Fig. 20. Validation and training and data across various epochs.

porosities (ε) and anisotropic angles (ω) at two snapshots: $t = 2000$ s and $t = 3000$ s, with Kn set at 0.3. The illustrations suggest an anisotropic angle of $\omega = 0°$ yields optimal melting efficiency. During the intermediate phase of the charging process, particularly during melting, a distinct region emerges with mid-level porosity values (around $\varepsilon \sim 0.925$), where MVF is at its lowest. Interestingly, a porosity value of $\varepsilon = 0.9$ achieves the peak MVF, while a higher porosity of $\varepsilon = 0.94$ delivers commendable MVF. Lower porous MF excels in effective thermal conductivity, while higher porosity MF favors enhanced natural convection circulation. Consequently, the benefits of $\varepsilon = 0.94$ become more evident at $t = 3000$ s than at $t = 2000$ s.

6. Conclusions

PCMs possess the intrinsic ability to store and release significant energy during melting and solidification processes, respectively. In the present study, the efficacy of using two layers of MF to enhance heat transfer in a thermal energy storage unit is meticulously examined. One of the MF layers is heterogeneous with engineered local properties in an anisotropic angle ω. The finite element method was applied to solve the governing equations representing the physical behavior of the energy storage unit. Mesh study and model verifications were performed to ensure the accuracy of the model and computations. Due to the high cost of simulations, an ANN was trained to learn the physical behavior of the system using 7838 sample data. The results were reported in the form of MVF graphs, stored energy, and isotherm contours and streamlines. The key findings of the study can be summarized as follows:

- The results encompass examining the effects of the anisotropic angle (ω) ranging between 0° and 90° and a defined porosity (ε) value within 0.9 to 0.975. The core findings underscore a profound impact of MF's average porosity on the melting duration, as evidenced by the dramatic 66 % decrease in melting time resulting from a mere 7.5 % porosity augmentation. Further, the interplay between the melting fraction, stored energy, and varying heterogeneous angles reveals that a 0° anisotropic angle yields optimal heat transfer dynamics due to its favorable thermal conductivity and permeability attributes.
- An essential breakthrough in this study comes from adopting neural network-based analytics. The computational demands associated with phase change heat transfer analyses are notably high, often

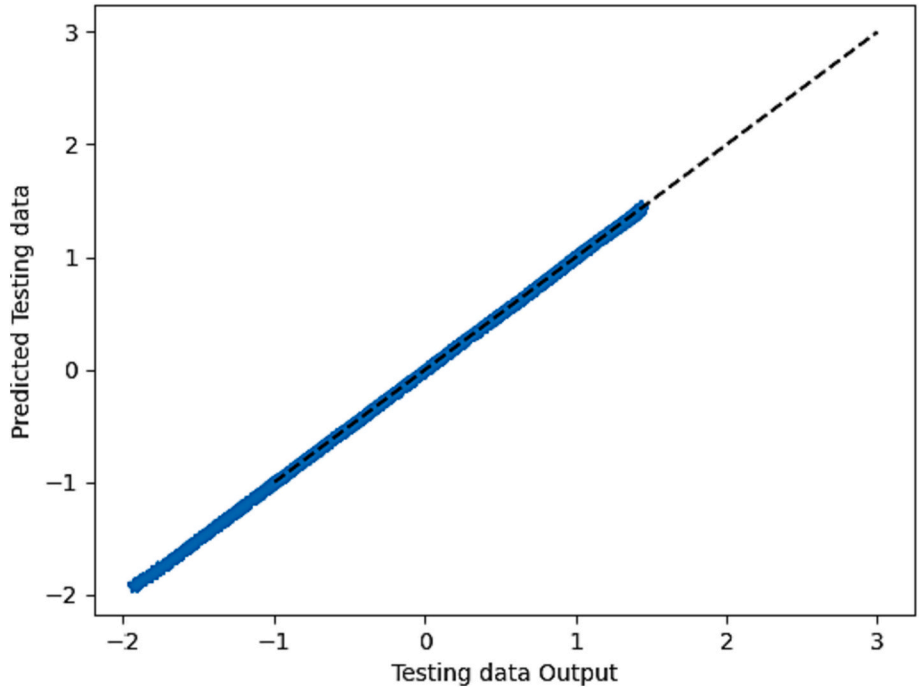

Fig. 21. Contrast of the actual test data with the predicted values.

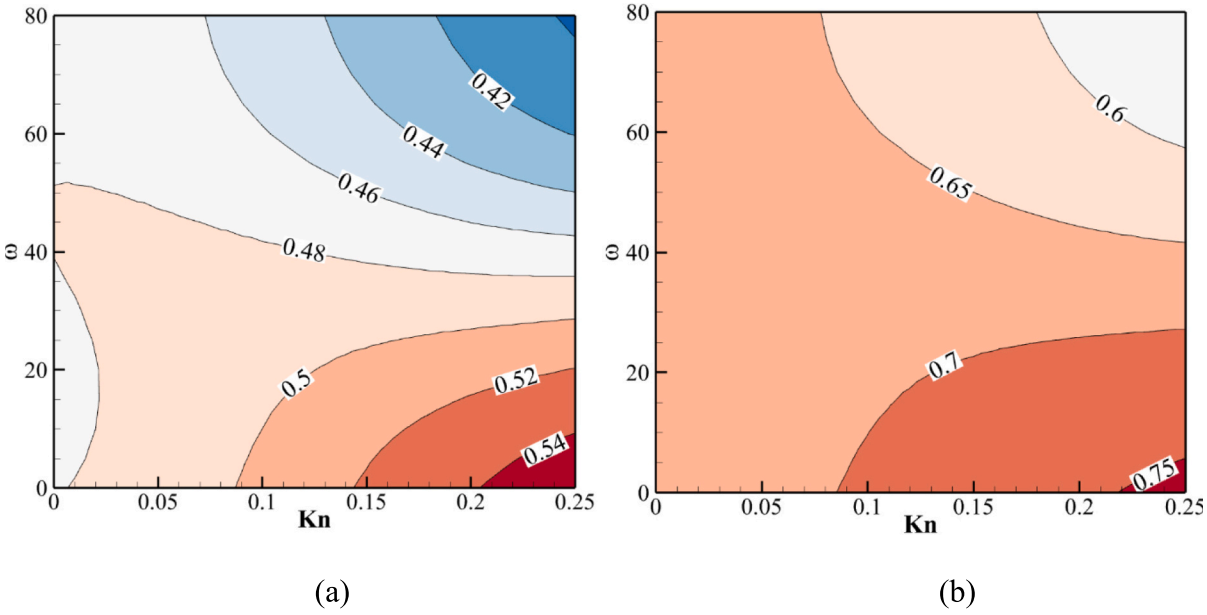

Fig. 22. Predicted *MVF* for various values of the heterogeneous parameter (*Kn*) and anisotropic angle (ω) when $\varepsilon = 0.9$ and for (a) $t = 2000$s and (b) $t = 3000$ s.

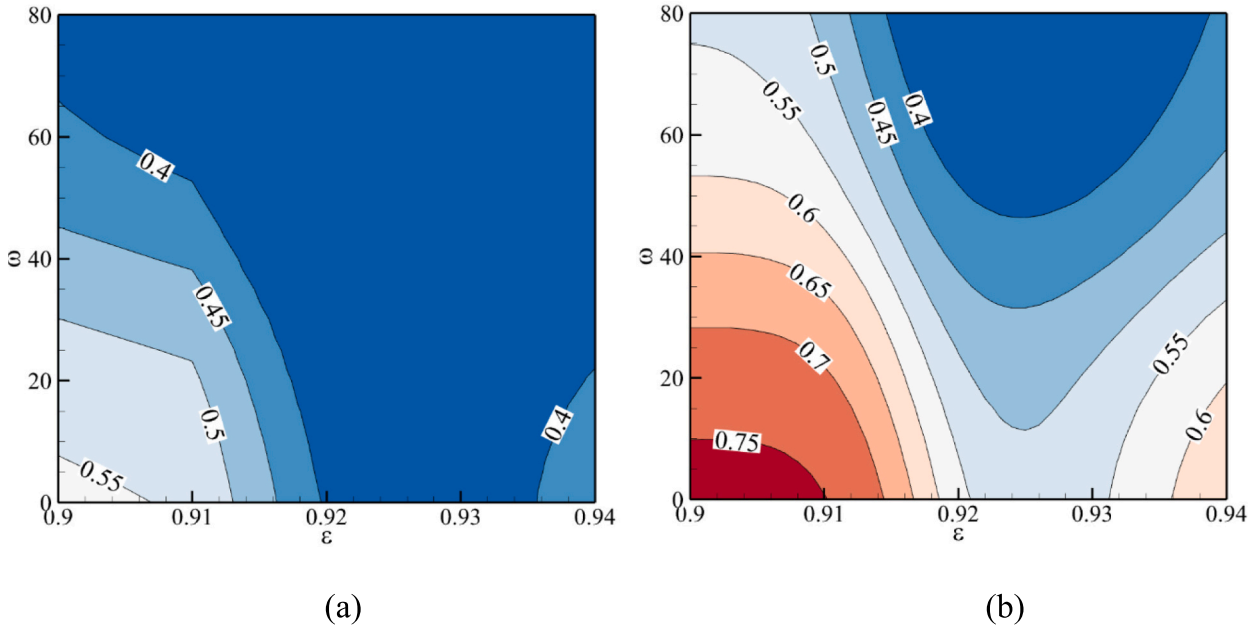

Fig. 23. Predicted *MVF* for various values of porosity (ε) and anisotropic angle (ω) when $Kn = 0.3$ and for (a) $t = 2000$s and (b) $t = 3000$ s.

making intricate investigations laborious. By integrating a neural network model, the researchers elucidated detailed heat transfer dynamics without the traditionally associated computational overheads. After rigorous training and validation phases, the model showcased its prowess by presenting the contours of MVF concerning varying control parameters, as highlighted in illustrative figures.

- Neural network analysis provided deeper understanding, highlighting the highest melting efficiencies at an anisotropic angle of $\omega = 0°$. This analysis revealed a clear area where MVF reaches its lowest point at a porosity level of approximately $\varepsilon = 0.925$. The advantages of a greater porosity, especially at $\varepsilon = 0.94$, were notably apparent for the extended observation period of $t = 3000$ s.

In essence, this comprehensive investigation merges traditional analytical methodologies with the prowess of neural networks, forging a deeper understanding of phase change heat transfer dynamics in PCM containers with embedded metal foam layers for thermal energy storage units. The revelations, especially about the nuanced effects of porosity and anisotropic angles, promise significant implications for designing advanced thermal energy storage systems, paving the way for more efficient and sustainable energy solutions.

CRediT authorship contribution statement

Hakim S. Sultan: Writing – review & editing, Supervision, Methodology, Formal analysis, Data curation, Conceptualization. **Mohammed Hasan Ali:** Writing – review & editing, Writing – original draft, Visualization, Software, Investigation, Formal analysis, Data curation. **Jana Shafi:** Writing – review & editing, Writing – original draft, Visualization, Software, Investigation, Formal analysis, Data curation.

Mehdi Fteiti: Writing – review & editing, Writing – original draft, Methodology, Investigation, Formal analysis. **Manuel Baro:** Writing – review & editing, Methodology, Investigation, Formal analysis. **Faisal Alresheedi:** Writing – original draft, Supervision, Methodology, Investigation, Formal analysis. **Mohammad S. Islam:** Writing – review & editing, Writing – original draft, Investigation, Formal analysis, Data curation. **Talal Yusaf:** Writing – review & editing, Investigation, Formal analysis. **Mohammad Ghalambaz:** Writing – review & editing, Methodology, Investigation.

Declaration of competing interest

The authors clarify that there is no conflict of interest for report.

Data availability

No data was used for the research described in the article.

Acknowledgments

The authors would like to thank the Deanship of Scientific Research at Umm Al-Qura University for supporting this work by Grant Code: (23UQU4310414DSR010).

References

[1] J.M. Panchal, K.V. Modi, V.J. Patel, Development in multiple-phase change materials cascaded low-grade thermal energy storage applications: a review, Clean. Eng. Technol. 8 (2022) 100465.
[2] N.I. Ibrahim, F.A. Al-Sulaiman, S. Rahman, B.S. Yilbas, A.Z. Sahin, Heat transfer enhancement of phase change materials for thermal energy storage applications: a critical review, Renew. Sust. Energ. Rev. 74 (2017) 26–50.
[3] W. Cui, T. Si, X. Li, X. Li, L. Lu, T. Ma, Q. Wang, Heat transfer enhancement of phase change materials embedded with metal foam for thermal energy storage: a review, Renew. Sust. Energ. Rev. 169 (2022) 112912.
[4] H.A. Ahmadi, N. Variji, A. Kaabinejadian, M. Moghimi, M. Siavashi, Optimal design and sensitivity analysis of energy storage for concentrated solar power plants using phase change material by gradient metal foams, J. Energy Storage 35 (2021) 102233.
[5] W. Liu, Y. Bie, T. Xu, A. Cichon, G. Królczyk, Z. Li, Heat transfer enhancement of latent heat thermal energy storage in solar heating system: a state-of-the-art review, J. Energy Storage 46 (2022) 103727.
[6] D. Ghosh, J. Ghose, P. Datta, P. Kumari, S. Paul, Strategies for phase change material application in latent heat thermal energy storage enhancement: status and prospect, J. Energy Storage 53 (2022) 105179.
[7] X. Wang, W. Li, Z. Luo, K. Wang, S.P. Shah, A critical review on phase change materials (PCM) for sustainable and energy efficient building: design, characteristic, performance and application, Energy Build. 260 (2022) 111923.
[8] W. Hua, L. Zhang, X. Zhang, Research on passive cooling of electronic chips based on PCM: a review, J. Mol. Liq. 340 (2021) 117183.
[9] M. Ghalambaz, J. Zhang, Conjugate solid-liquid phase change heat transfer in heatsink filled with phase change material-metal foam, Int. J. Heat Mass Transf. 146 (2020) 118832.
[10] P.T. Sardari, R. Babaei-Mahani, D. Giddings, S. Yasseri, M. Moghimi, H. Bahai, Energy recovery from domestic radiators using a compact composite metal Foam/PCM latent heat storage, J. Clean. Prod. 257 (2020) 120504.
[11] P.T. Sardari, D. Grant, D. Giddings, G.S. Walker, M. Gillott, Composite metal foam/PCM energy store design for dwelling space air heating, Energy Convers. Manag. 201 (2019) 112151.
[12] A. Alhusseny, N. Al-Zurfi, A. Nasser, A. Al-Fatlawi, M. Aljanabi, Impact of using a PCM-metal foam composite on charging/discharging process of bundled-tube LHTES units, Int. J. Heat Mass Transf. 150 (2020) 119320.
[13] C. Nie, J. Liu, S. Deng, Effect of geometry modification on the thermal response of composite metal foam/phase change material for thermal energy storage, Int. J. Heat Mass Transf. 165 (2021) 120652.
[14] M. Aramesh, B. Shabani, Metal foam-phase change material composites for thermal energy storage: a review of performance parameters, Renew. Sust. Energ. Rev. 155 (2022) 111919.
[15] Q. Ying, H. Wang, E. Lichtfouse, Numerical simulation on thermal behavior of partially filled metal foam composite phase change materials, Appl. Therm. Eng. 229 (2023) 120573.
[16] M.A. Fteiti, M. Ghalambaz, O. Younis, M. Sheremet, M. Ismael, The influence of the metal foam layer shape on the thermal charging response time of a latent heat thermal energy storage system, J. Energy Storage 58 (2023) 106284.
[17] M. Ghalambaz, A.A. Melaibari, A.J. Chamkha, O. Younis, M. Sheremet, Phase change heat transfer and energy storage in a wavy-tube thermal storage unit filled with a nano-enhanced phase change material and metal foams, J. Energy Storage 54 (2022) 105277.
[18] V. Joshi, M.K. Rathod, Thermal transport augmentation in latent heat thermal energy storage system by partially filled metal foam: a novel configuration, J. Energy Storage 22 (2019) 270–282.
[19] V. Joshi, M.K. Rathod, Thermal performance augmentation of metal foam infused phase change material using a partial filling strategy: an evaluation for fill height ratio and porosity, Appl. Energy 253 (2019) 113621.
[20] S. Mehryan, K.A. Ayoubloo, M. Mahdavi, O. Younis, Z. Kazemi, M. Ghodrat, M. Ghalambaz, Optimum configuration of a metal foam layer for a fast thermal charging energy storage unit: a numerical study, J. Energy Storage 48 (2022) 103950.
[21] A. Mirshekar, M.R. Goodarzi, D. Mohebbi-Kalhori, M.H.S. Mayam, Experimental study of heat transfer enhancement using metal foam partially filled with phase change material in a heat sink, J. Energy Storage 60 (2023) 106496.
[22] J. Zou, X. Meng, Investigating the effect of distribution form of copper foam fins on the thermal performance improvement of latent thermal energy storage units, Int. Commun. Heat Mass Transf. 141 (2023) 106571.
[23] Y. Gao, F. Liu, J. Wang, W. Ye, X. Meng, Influence of the copper foam shape on thermal performance of phase-change material, J. Energy Storage 36 (2021) 102416.
[24] X. Meng, L. Yan, F. He, Filling copper foam partly on thermal behavior of phase-change material in a rectangular enclosure, J. Energy Storage 32 (2020) 101867.
[25] X. Meng, L. Yan, J. Xu, F. He, H. Yu, M. Zhang, Effect of porosity and pore density of copper foam on thermal performance of the paraffin-copper foam composite Phase-Change Material, Case Stud. Therm. Eng. 22 (2020) 100742.
[26] X. Meng, L. Meng, J. Zou, F. He, Influence of the copper foam fin (CFF) shapes on thermal performance of phase-change material (PCM) in an enclosed cavity, Case Stud. Therm. Eng. 23 (2021) 100810.
[27] X. Meng, S. Liu, J. Zou, F. Liu, J. Wang, Inclination angles on the thermal behavior of Phase-Change Material (PCM) in a cavity filled with copper foam partly, Case Stud. Therm. Eng. 25 (2021) 100944.
[28] S. Christopher, K. Parham, A. Mosaffa, M. Farid, Z. Ma, A.K. Thakur, H. Xu, R. Saidur, A critical review on phase change material energy storage systems with cascaded configurations, J. Clean. Prod. 283 (2021) 124653.
[29] M.-J. Li, M.-J. Li, X.-D. Xue, D. Li, Optimization and design criterion of the shell-and-tube thermal energy storage with cascaded PCMs under the constraint of outlet threshold temperature, Renew. Energy 181 (2022) 1371–1385.
[30] C. Yang, Y. Xu, X. Cai, Z.-J. Zheng, Melting behavior of the latent heat thermal energy storage unit with fins and graded metal foam, Appl. Therm. Eng. 198 (2021) 117462.
[31] F. Zhu, C. Zhang, X. Gong, Numerical analysis on the energy storage efficiency of phase change material embedded in finned metal foam with graded porosity, Appl. Therm. Eng. 123 (2017) 256–265.
[32] M. Ghalambaz, M. Aljaghtham, A.J. Chamkha, A. Abdullah, A. Alshehri, M. Ghalambaz, Anisotropic metal foam design for improved latent heat thermal energy storage in a tilted enclosure, Int. J. Mech. Sci. 238 (2023) 107830.
[33] M. Ghalambaz, M. Aljaghtham, A.J. Chamkha, A. Abdullah, I. Mansir, M. Ghalambaz, Mathematical modeling of heterogeneous metal foams for phase-change heat transfer enhancement of latent heat thermal energy storage units, Appl. Math. Model. 115 (2023) 398–413.
[34] P.T. Sardari, H.I. Mohammed, D. Giddings, M. Gillott, D. Grant, Numerical study of a multiple-segment metal foam-PCM latent heat storage unit: effect of porosity, pore density and location of heat source, Energy 189 (2019) 116108.
[35] G. Liu, T. Xiao, P. Wei, X. Meng, X. Yang, J. Yan, Y.-L. He, Experimental and numerical studies on melting/solidification of PCM in a horizontal tank filled with graded metal foam, Sol. Energy Mater. Sol. Cells 250 (2023) 112092.
[36] Y. Zhuang, Z. Liu, W. Xu, Effects of gradient porous metal foam on the melting performance and energy storage of composite phase change materials subjected to an internal heater: a numerical study and PIV experimental validation, Int. J. Heat Mass Transf. 183 (2022) 122081.
[37] M.H.S. Abandani, D.D. Ganji, Melting effect in triplex-tube thermal energy storage system using multiple PCMs-porous metal foam combination, J. Energy Storage 43 (2021) 103154.
[38] J.M. Mahdi, H.I. Mohammed, E.T. Hashim, P. Talebizadehsardari, E.C. Nsofor, Solidification enhancement with multiple PCMs, cascaded metal foam and nanoparticles in the shell-and-tube energy storage system, Appl. Energy 257 (2020) 113993.
[39] J. Shafi, M. Sheremet, M. Fteiti, A.M. Saeed, M. Ghalambaz, Computational study of phase change heat transfer and latent heat energy storage for thermal management of electronic components using neural networks, Mathematics 11 (2) (2023) 356.
[40] K. Venkateshwar, S. Tasnim, S. Gadsden, S. Mahmud, Artificial neural network-genetic algorithm optimized graded metal foam, J. Energy Storage 51 (2022) 104386.
[41] M. Edalatifar, M.B. Tavakoli, M. Ghalambaz, F. Setoudeh, Using deep learning to learn physics of conduction heat transfer, J. Therm. Anal. Calorim. 146 (2021) 1435–1452.
[42] M. Edalatifar, M. Ghalambaz, M.B. Tavakoli, F. Setoudeh, New loss functions to improve deep learning estimation of heat transfer, Neural Comput. & Applic. 34 (18) (2022) 15889–15906.
[43] M. Ghalambaz, M. Edalatifar, S. Moradi Maryamnegari, M. Sheremet, An intelligence parameter classification approach for energy storage and natural convection and heat transfer of nano-encapsulated phase change material: deep neural networks, Neural Comput. & Applic. (2023) 1–9.
[44] W. Cui, T. Si, X. Li, X. Li, L. Lu, T. Ma, Q. Wang, Heat transfer analysis of phase change material composited with metal foam-fin hybrid structure in inclination

container by numerical simulation and artificial neural network, Energy Rep. 8 (2022) 10203–10218.
[45] P. Yu, Y. Wang, R. Ji, H. Wang, J. Bai, Pore-scale numerical study of flow characteristics in anisotropic metal foam with actual skeleton structure, Int. Commun. Heat Mass Transf. 126 (2021) 105401.
[46] Q. Ren, Z. Wang, T. Lai, J. Zhang, Z. Qu, Conjugate heat transfer in anisotropic woven metal fiber-phase change material composite, Appl. Therm. Eng. 189 (2021) 116618.
[47] M. Bamdezh, G. Molaeimanesh, S. Zanganeh, Role of foam anisotropy used in the phase-change composite material for the hybrid thermal management system of lithium-ion battery, J. Energy Storage 32 (2020) 101778.
[48] M. Ghalambaz, M. Aljaghtham, A.J. Chamkha, A. Abdullah, A. Alshehri, M. Ghalambaz, An anisotropic metal foam design for improved latent heat thermal energy storage in a tilted enclosure, Int. J. Mech. Sci. 107830 (2022).
[49] J. Shafi, M. Ghalambaz, M. Fteiti, M. Ismael, M. Ghalambaz, Computational modeling of latent heat thermal energy storage in a shell-tube unit: using neural networks and anisotropic metal foam, Mathematics 10 (24) (2022) 4774.
[50] S. Zhang, Y. Yao, Y. Jin, Z. Shang, Y. Yan, Heat transfer characteristics of ceramic foam/molten salt composite phase change material (CPCM) for medium-temperature thermal energy storage, Int. J. Heat Mass Transf. 196 (2022) 123262.
[51] D.A. Nield, A. Bejan, Convection in Porous Media, Springer, 2006.
[52] Y. Yao, H. Wu, Interfacial heat transfer in metal foam porous media (MFPM) under steady thermal conduction condition and extension of Lemlich foam conductivity theory, Int. J. Heat Mass Transf. 169 (2021) 120974.
[53] C. Zhao, J. Wang, Y. Sun, S. He, K. Hooman, Fin design optimization to enhance PCM melting rate inside a rectangular enclosure, Appl. Energy 321 (2022) 119368.
[54] A.I.N. Korti, H. Guellil, Experimental study of the effect of inclination angle on the paraffin melting process in a square cavity, J. Energy Storage 32 (2020) 101726.
[55] A. Agarwal, R. Sarviya, Characterization of commercial grade paraffin wax as latent heat storage material for solar dryers, Mater. Today Proc. 4 (2) (2017) 779–789.
[56] N. Ukrainczyk, S. Kurajica, J. Šipušić, Thermophysical comparison of five commercial paraffin waxes as latent heat storage materials, Chem. Biochem. Eng. Q. 24 (2) (2010) 129–137.
[57] O.C. Zienkiewicz, R.L. Taylor, P. Nithiarasu, The Finite Element Method for Fluid Dynamics, Seventh Edition ed., Butterworth-Heinemann, Oxford, 2014.
[58] D. Pepper, The Intermediate Finite Element Method: Fluid Flow and Heat Transfer Applications, Routledge, 2017.
[59] C.T. Kelley, Solving Nonlinear Equations With Newton's Method, SIAM, 2003.
[60] P. Deuflhard, Newton Methods for Nonlinear Problems: Affine Invariance and Adaptive Algorithms, Springer Science & Business Media, 2005.
[61] M. Bollhöfer, O. Schenk, R. Janalik, S. Hamm, K. Gullapalli, State-of-the-art sparse direct solvers, in: Parallel Algorithms in Computational Science and Engineering, 2020, pp. 3–33.
[62] M. Bollhöfer, A. Eftekhari, S. Scheidegger, O. Schenk, Large-scale sparse inverse covariance matrix estimation, SIAM J. Sci. Comput. 41 (1) (2019) A380–A401.
[63] H. Zheng, C. Wang, Q. Liu, Z. Tian, X. Fan, Thermal performance of copper foam/paraffin composite phase change material, Energy Convers. Manag. 157 (2018) 372–381.
[64] I.K.M. Jais, A.R. Ismail, S.Q. Nisa, Adam optimization algorithm for wide and deep neural network, Knowl. Eng. Data Sci. 2 (1) (2019) 41–46.
[65] Scikit-Learn, sklearn.preprocessing.StandardScaler, in: Scikit-Learn, 2023.